Supporting Information for

# Shape-Programmed Fabrication and Actuation of Magnetically Active Micropost Arrays

*Jisoo Jeon,*[†] *Jeong Eun Park,*[†] *Sei Jin Park,*[‡] *Sukyoung Won,*[†] *Hangbo Zhao,*[§] *Sanha Kim,*[§] *Bong Sup Shim,*[∥] *Augustine Urbas,*[⊥] *A. John Hart,**[,§] *Zahyun Ku,**[,⊥] *Jeong Jae Wie**[,†]

[†]Department of Polymer Science and Engineering, Inha University, Incheon 22212, South Korea

[‡]Physical and Life Sciences Directorate, Lawrence Livermore National Laboratory, Livermore, California 94550, United Stages

[§]Department of Mechanical Engineering and Laboratory for Manufacturing and Productivity, Massachusetts Institute of Technology, Cambridge, Massachusetts 02139, United States

[∥]Department of Chemical Engineering, Inha University, Incheon 22212, South Korea

[⊥]Materials and Manufacturing directorate, Air Force Research Laboratory, Wright-Patterson Air Force Base, Ohio 45433, United States

**Corresponding Author**

*J. J. Wie. E-mail: wie@inha.ac.kr

*Z. Ku. E-mail: zahyun.ku.1.ctr@us.af.mil

*A. J. Hart. E-mail: ajhart@mit.edu

**Size distribution and diameter**

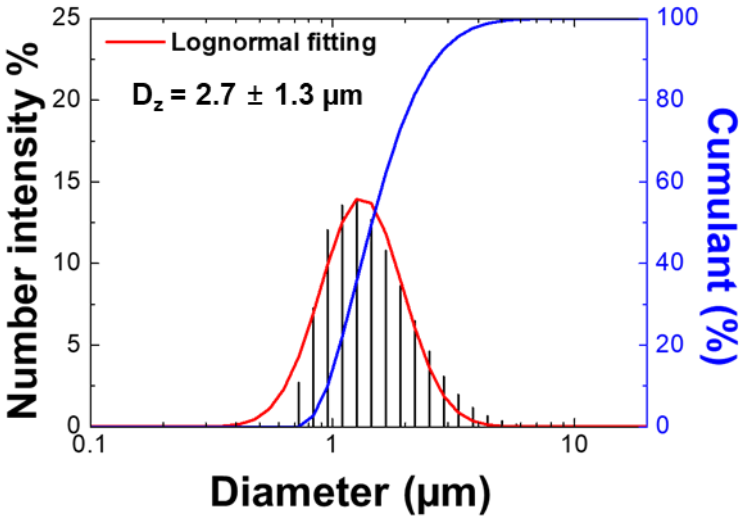


**Figure S1.** Size distribution of the carbonyl iron particles; black histograms are the number intensity, blue line is the cumulant of number intensity, and red line is the lognormal fitting of the size distribution of particles.

The calculated z-averaged diameter ($D_z$) is based on particle size analyzer (PSA) by applying equation below[1].

$$D_z = < d > \frac{[z+3][z+2]}{[z+1]^2} \quad \text{(S1)}$$

$$z = \frac{1}{p^2} - 1 \quad \text{(S2)}$$

$$p = \left(\frac{Standard\ deviation}{mean\ value}\right) = \left(\frac{\sigma}{\mu}\right) \quad \text{(S3)}$$

$< d >$ is the mean diameter and $p$ is the polydispersity index, corresponding to the standard deviation, $\sigma$, divided by the mean value of the number-averaged diameter of the iron particles.

**Geometry of iron particle**

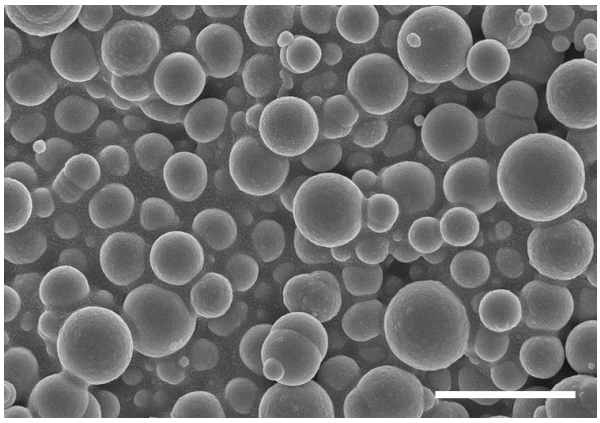

**Figure S2.** SEM micrograph of the carbonyl iron particles (Scale bar: 3 μm).

We confirmed that the iron particles have spherical shapes by the SEM micrograph.

The carbonyl iron particle is composed of iron (Fe) over 97%, and the magnetic properties of carbonyl iron particles, we have used, are described in previously report [2,3].

**Finite element analysis**

A finite element analysis of the structural deformation due to external magnetic fields was performed using Ansys Mechanical APDL 19.0 software. The semi-cylindrical structure was modeled using SOLID 186 elements with approximate size of $3 \times 3 \times 3$ $\mu m^3$ to conserve computational power (results were verified against $1 \times 1 \times 1$ $\mu m^3$ element sizes and match well) and material properties of PDMS. In the presence of a strong external magnetic field, the iron particle array is magnetized and exhibit magnetic dipole moment. Since this magnetic moment is misaligned with the external magnetic field direction, the induced magnetic dipole experiences a torque ($\tau$):

$$\tau = m \times B \quad \text{(S4)}$$

where m is the magnetic dipole moment and B is the external magnetic field. For the finite element analysis, the resulting torque was converted to force and distributed across the

structure according to the iron particle array direction. A correction factor was applied to the resulting forces that accounts for the initial non-linear magnetization as well as saturation at high magnetizing force of ferromagnetic materials as shown in Figure S5 below.

To capture the changes in the torque depending on the orientation of the magnetic dipole which changes as the result of the deformation, the forces were applied in small increments (No. of steps = 50) and iterative solution and updating of the structure geometry and the direction and magnitude of the forces was successively performed to emulate the physical transformation the pillars undergo. Due to small incremental changes in the deformed shape, the material properties were assumed to be linear elastic. The resulting deformed geometries for bending and twisting structures are shown in Figure S8 below.

Using this framework, geometric characteristics such as bending and twisting angles can be calculated depending on the strength and relative orientation of the magnetic field to the nanoparticle array, enabling predictive synthesis and actuation of the pillars. In addition, the framework developed here allows for in depth examination of the internal stress distributions to understand and suppress failure mechanisms should the structures fail in service.

**Calculation of the bending stiffness**

Bending stiffness (k) of micropillar is calculated by following equation [4].

$$\mathrm{k} = \frac{3EI}{L^3} \tag{S5}$$

*E* is the elastic modulus of materials, *I* is the second moment of inertia, and *L* is length of micropillar. *E* and *L* is fixed from the identical material and geometry (E: 1.2 MPa (VA micropillar) and L: 60 μm). The second moment of inertia of semicircle is determined by the radius and neutral axis of the micropillar as following equations.

$$\text{A-(i):}\ I_\theta = \left(\frac{\pi}{8} - \frac{8}{9\pi}\right) r^4 \ \ (\theta = 0, \pi) \tag{S6}$$

$$\text{A-(ii): } I_\theta = I_0 - Ad^2 \quad \left(\theta \neq \frac{\pi}{2}n\right) \tag{S7}$$

$$\text{A-(iii): } I_\theta = \frac{\pi r^4}{8} \quad \left(\theta = \frac{\pi}{2}, \frac{3}{2}\pi\right) \tag{S8}$$

$d$ is distance between neutral axis and flat edge, A is area of the cross-sectional surface. The second moment of inertia ($I_\theta$) divides with three regions by the offset angle (Figure S10a). In case of Figure S10b, neutral axis located at centroid of the semicircle in tilted state, and calculated as following equation.

$$\left(\frac{\pi-\theta}{2}\right)r^2 + asin\left(\frac{d}{r}\right)r^2 + d(r^2-d^2)^{\frac{1}{2}} + d^2\,tan\left(\theta-\frac{\pi}{2}\right) = \frac{r^2}{2}\left(\theta-\frac{\pi}{2}\right) + \frac{\pi r^2}{4} \tag{S9}$$

The calculated bending stiffness is minimized when bending direction is parallel to horizontally short axis, and maximized when bending direction is parallel to horizontally long axis (Figure S10d).

To generate multi-modal magnetic actuation, we rotate the microarray and measure the actuation angle. The offset angle set as the angle between magnetic field and horizontally short axis. Degree of actuation is calculated by the equation below

$$Degree\ of\ bending = \frac{number\ of\ bent\ pillar}{total\ pillar}$$

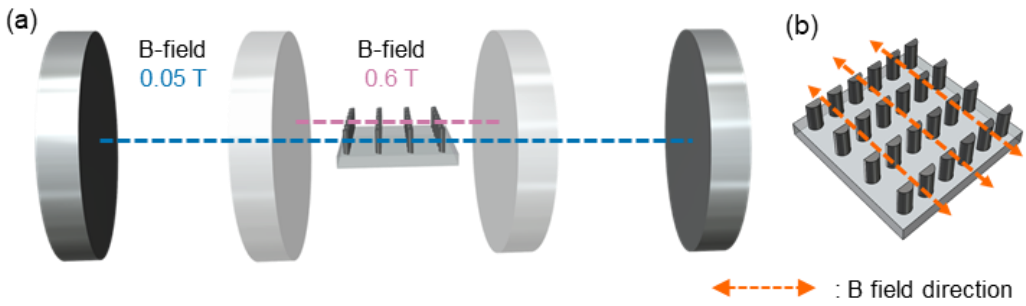


**Figure S3.** Linear magnetic field for actuation. (a) Magnetic field generation with distance adjustment between two permanent magnets. (b) Direction of the applied magnetic field with respect to the sample

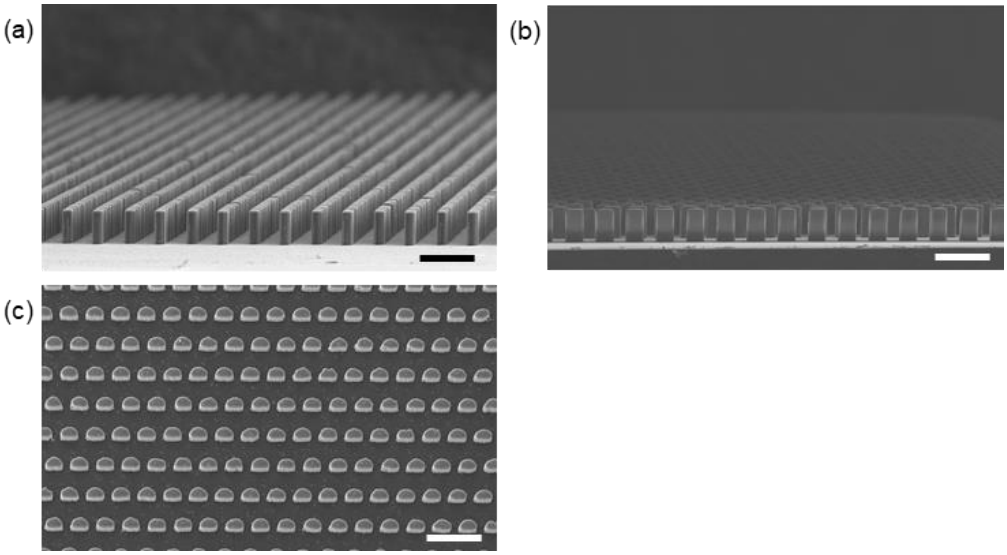


**Figure S4.** SEM micrographs of the geometry of microarrays. (a) Side view to thin width of micropillar. (b) Side view to thick width of micropillar. (c) Top-down view of microarray. (Scale bars: 100 μm)

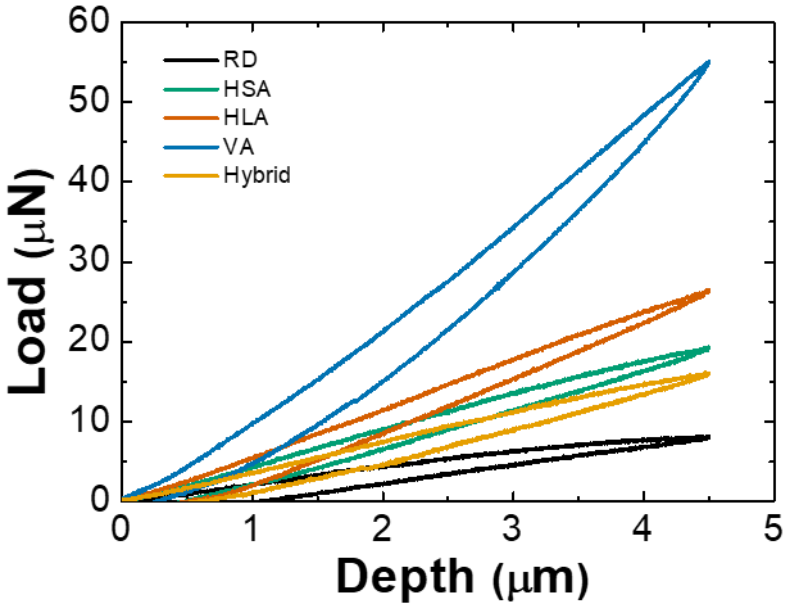


**Figure S5.** Mechanical properties of each micropillars. Loading/unloading curves of each micropillars measured by nanoindentation using a 10 μm diameter sized sapphire tip.

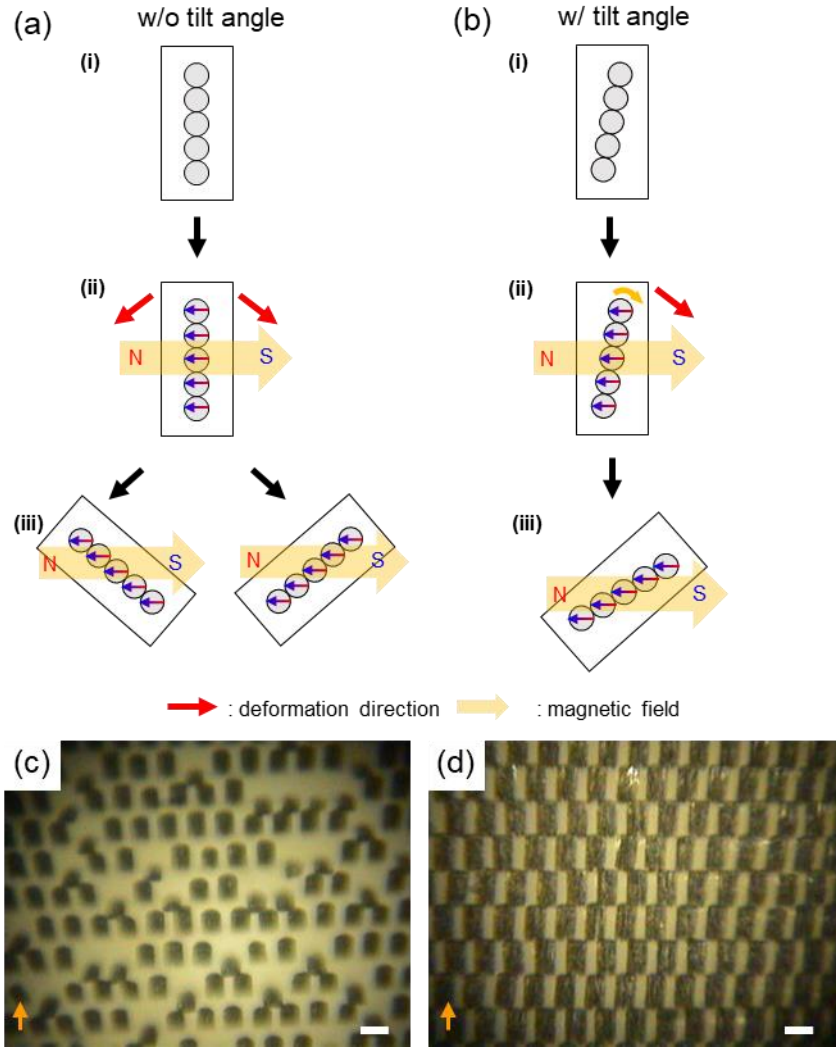


**Figure S6.** The mechanism of uniform actuation with tilt angle in particle alignment. (a) Schematic images of magnetic response of magnetic composites without tilt angle. (i) Without magnetic field, (ii) Magnetization of aligned iron particles by external magnetic field, (iii) Randomly directional deformation (b) Schematic images of magnetic response of magnetic composites with tilt angle. (i) Without magnetic field, (ii) magnetization of aligned iron particles by external magnetic field, (iii) unidirectional deformation (c) The actuation of VA microarray without tilt angle in particle alignment. (d) The actuation of VA microarray with tilt angle in particle alignment. (magnetic flux density: 0.6 T, scale bars: 50 μm)

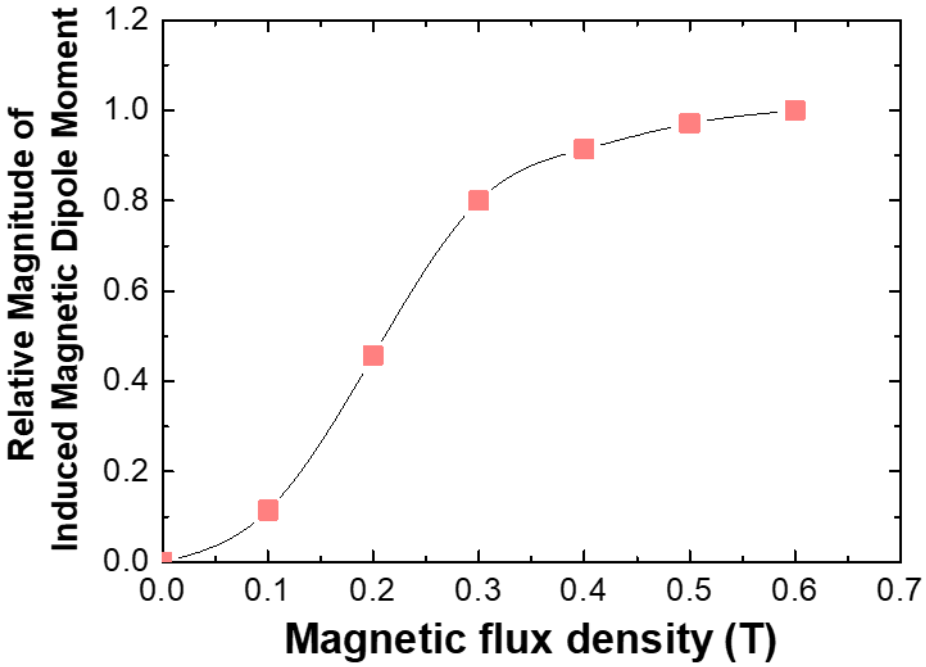


**Figure S7.** Correction factor for finite elemental method (FEM) simulation. Forces acting on the model was adjusted using the relative magnitude of induced dipole moment to reflect non-linear scaling with magnetizing field flux density.

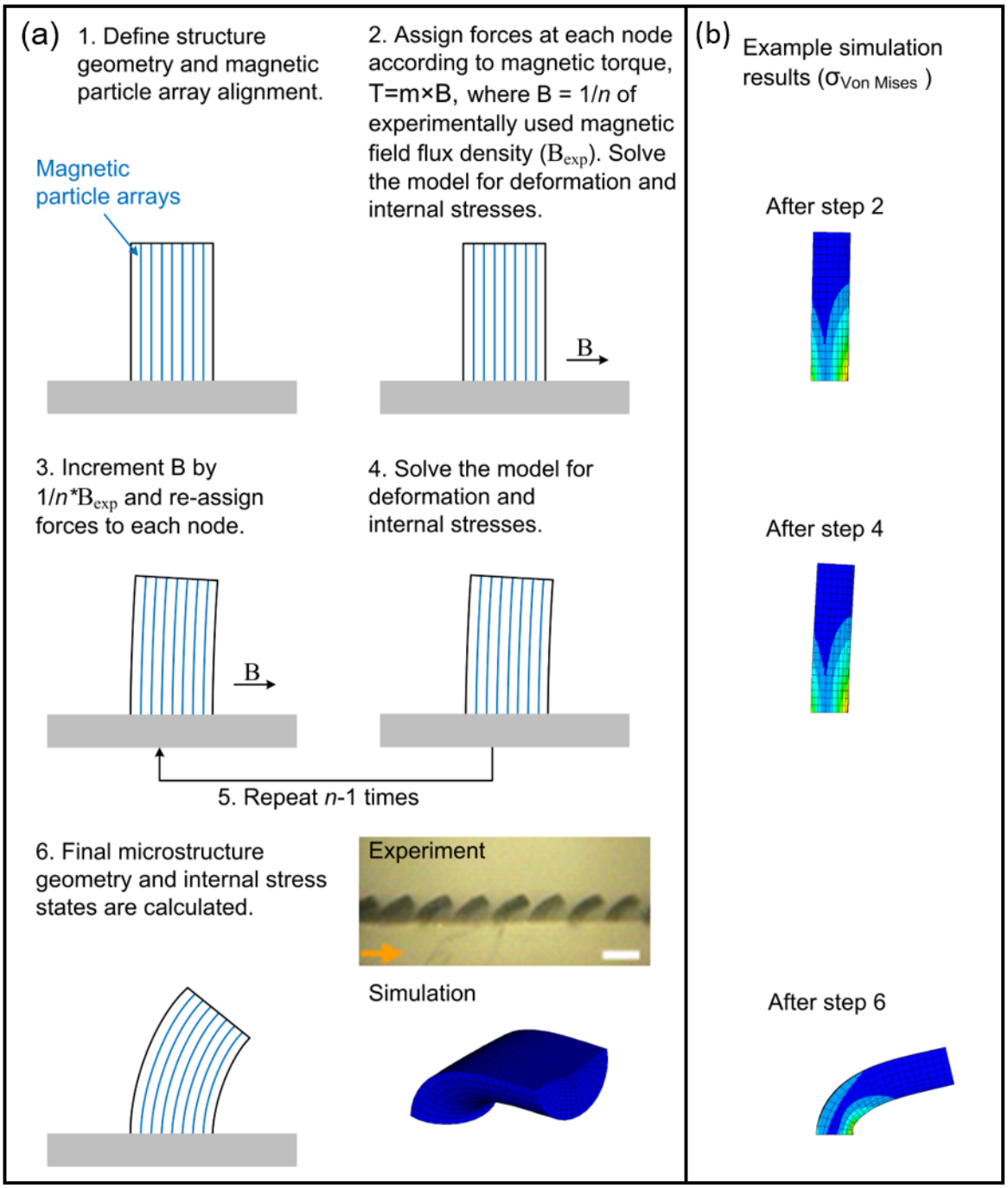


**Figure S8**. Procedure of FEM simulation. (a) Step of FEM simulation with (b) the Vol Mises stress distribution

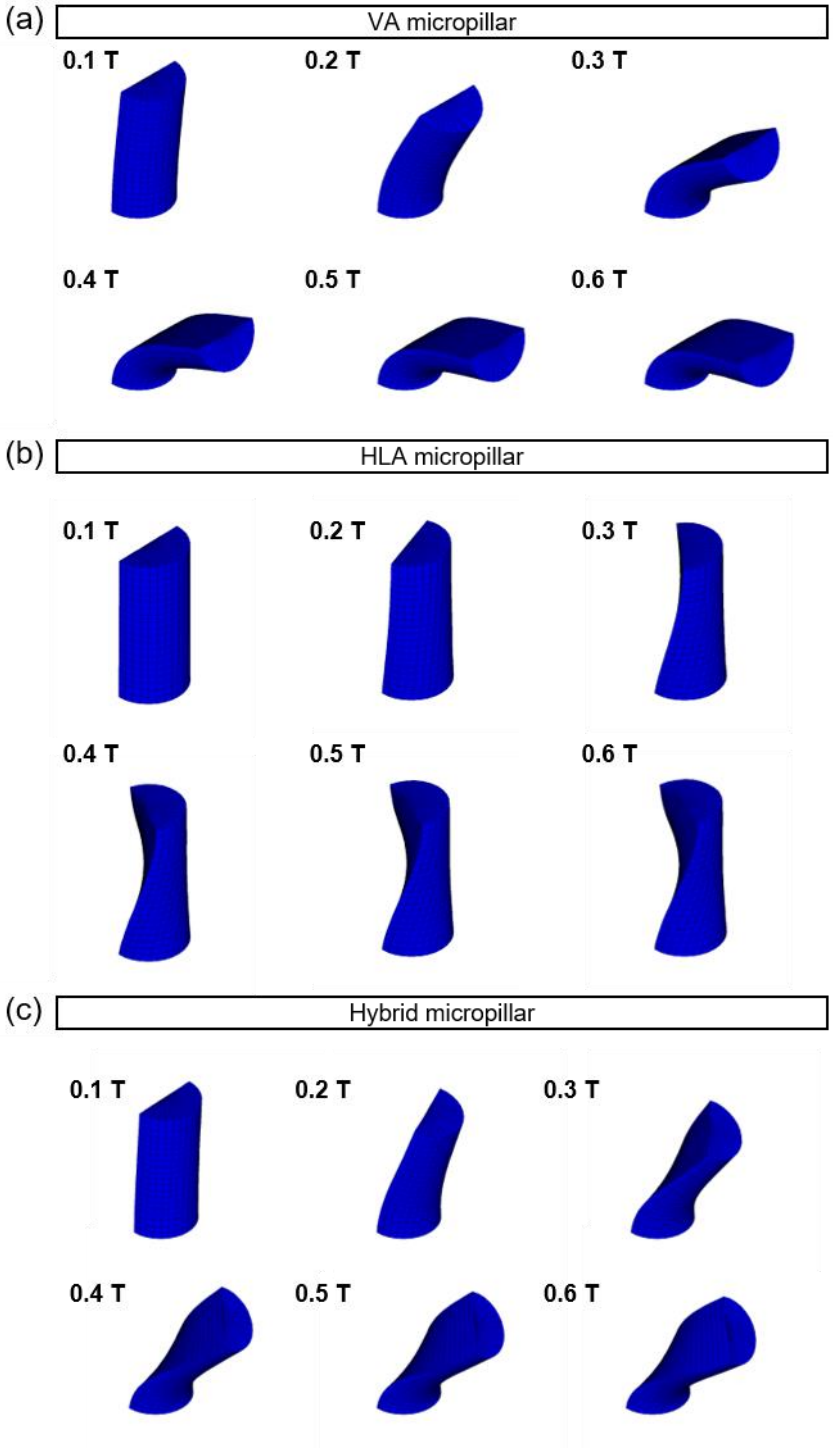


**Figure S9.** Deformed structure plots at different magnetic flux density. (a) Bending structure. (b) Twisting structures. (c) Simultaneously bending and twisting (hybrid) structures.

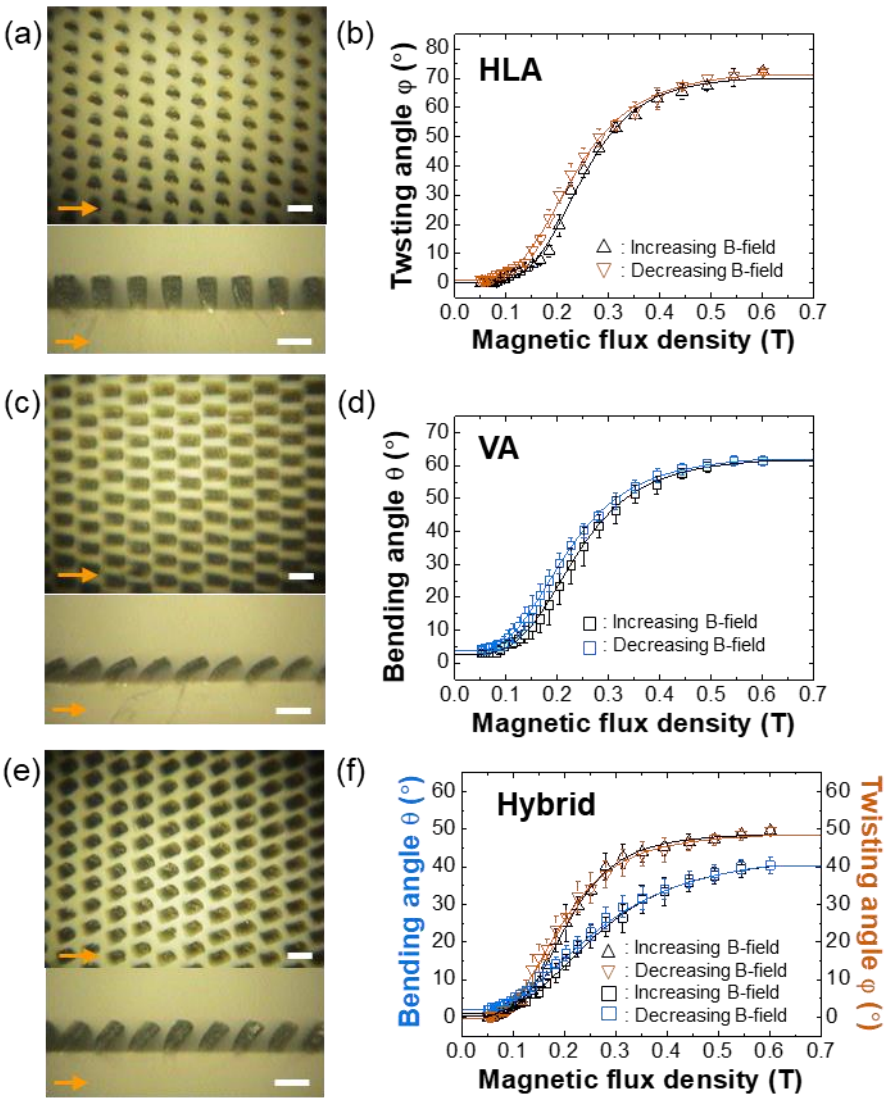


**Figure S10.** Magnetic hysteresis of actuation in each microarray. (a, c, e) Top-down (upper) & side (bottom) view of micropillar arrays upon actuation. Orange arrows mean direction of magnetic field. (Scale bars: 50 μm) (b, d, f) The difference of actuation angle between increasing and decreasing magnetic flux density (a, b: HLA microarray, c, d: VA microarray, e, f: hybrid microarray)

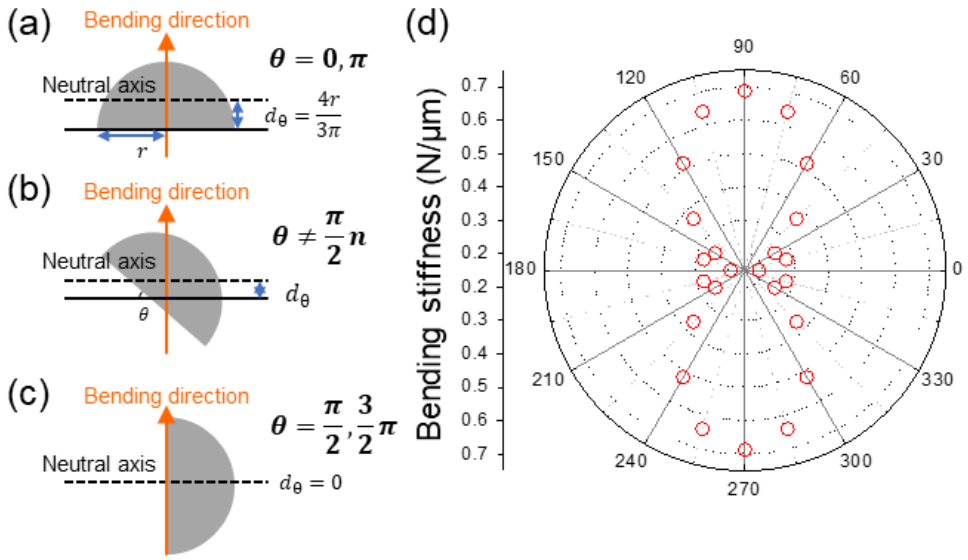


**Figure S11.** Bending stiffness of the semi-circular micropillar. (a, b, c) The schematic image of parameters according to the bending directions. (a) Horizontally short axis. (b) The axis which not including (a) and (b). (c) Horizontally long axis. (d) Bending stiffness of semicircular pillar varied with offset angle between horizontally short axis and bending direction.

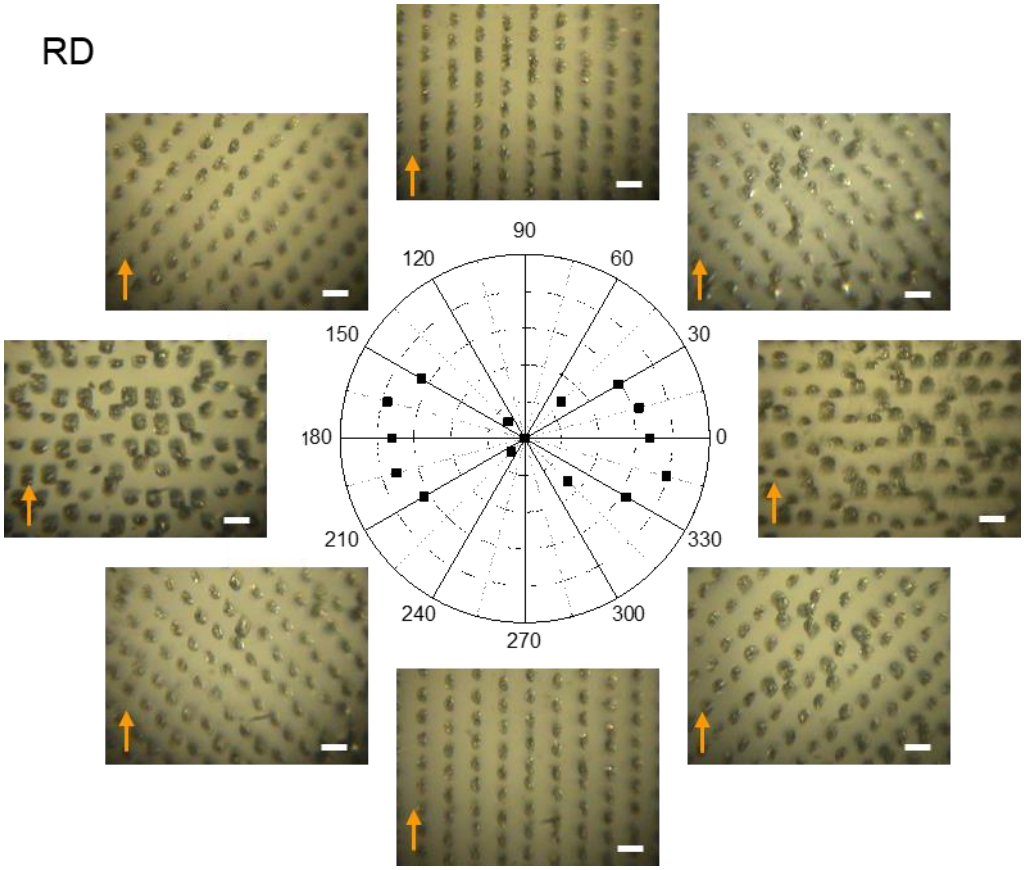


**Figure S12.** The effect of bending stiffness variation. Degree of actuation through varying offset angle between magnetic field direction and horizontally short axis of micropillar. (Scale bars: 50 μm)

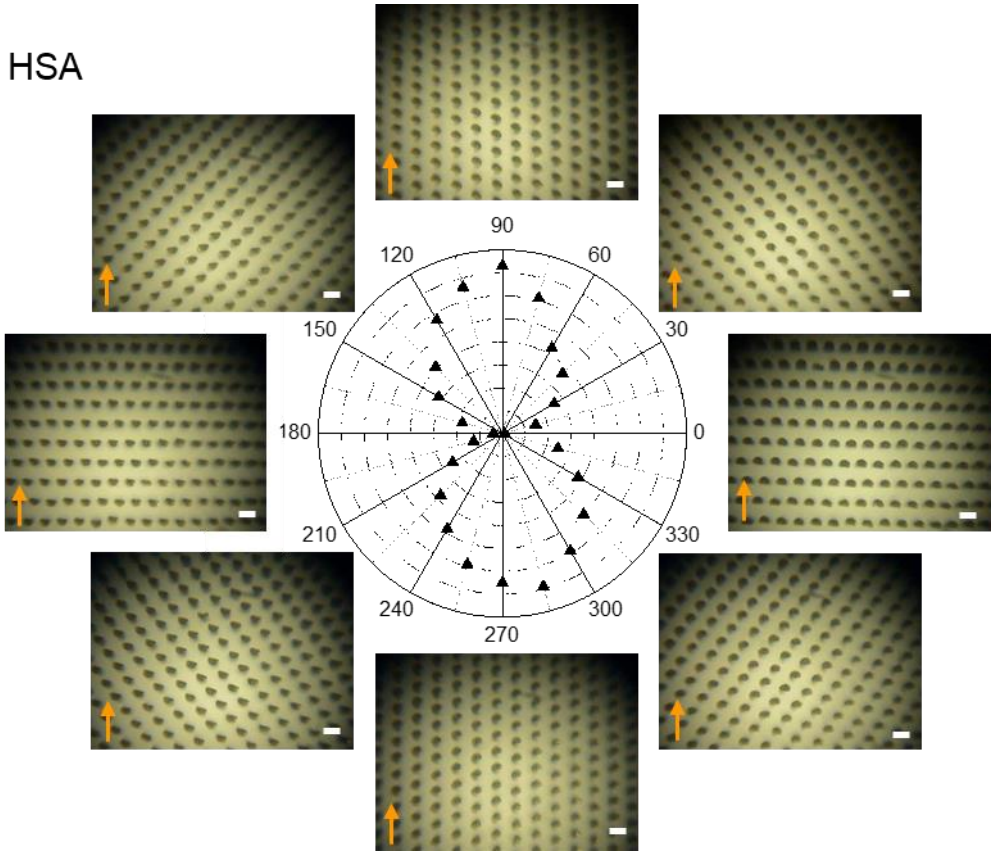


**Figure S13.** The twisting angle variation of HSA microarray. Polar plot of twisting angle of HSA microarray depends on offset angle between horizontally short axis and magnetic field direction. (Scale bars: 50 μm)

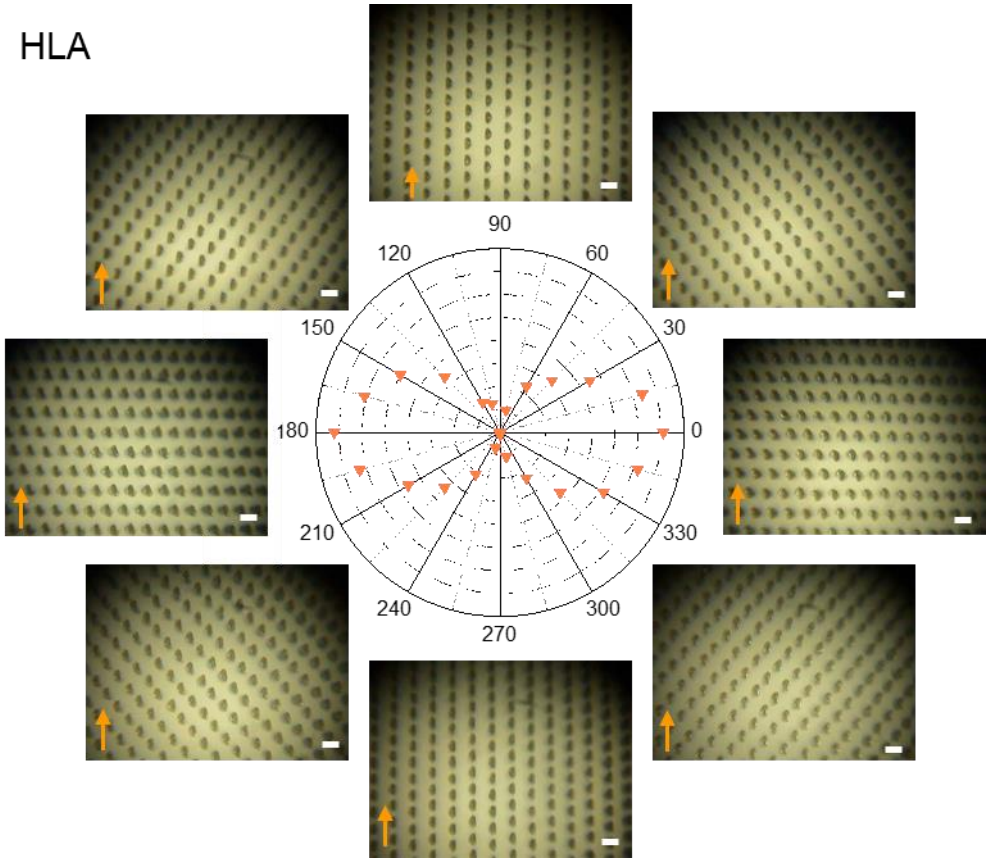


**Figure S14.** The twisting angle variation of HLA microarray with offset angle. Polar plot of twisting angle of HLA microarray depends on offset angle between horizontally short axis and magnetic field direction. (Scale bars: 50 μm)

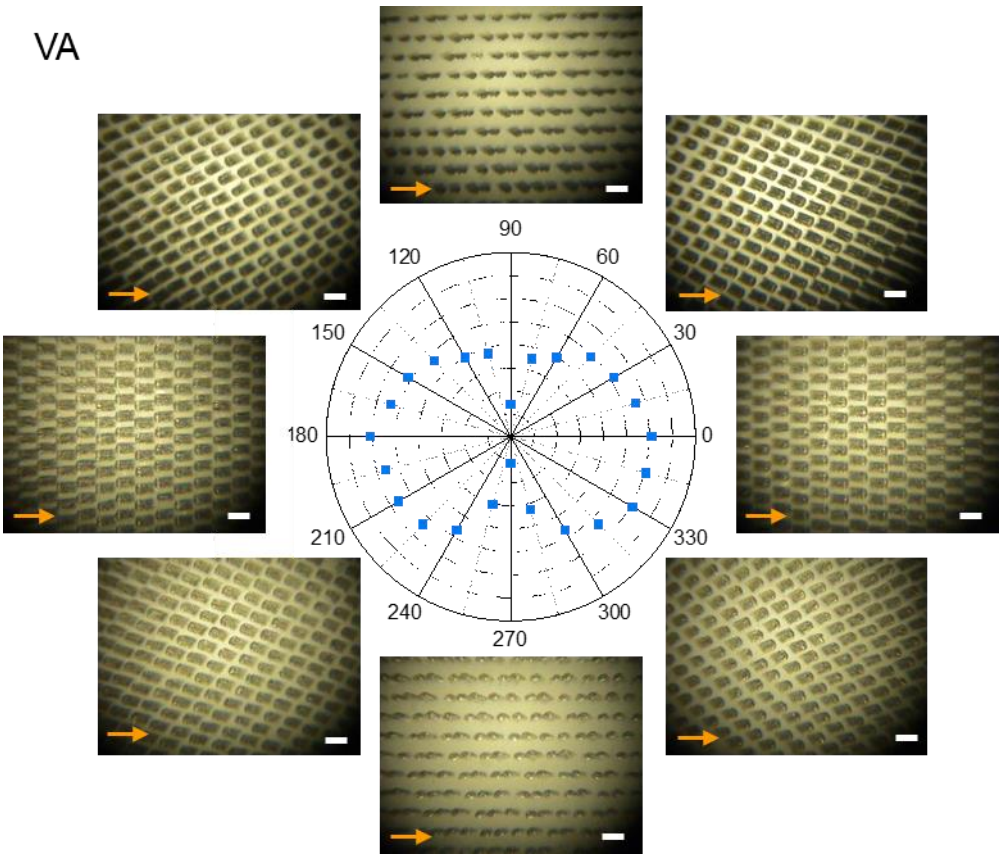


**Figure S15.** The bending angle variation of VA microarray with offset angle. Polar plot of bending angle of VA microarray depends on offset angle between horizontally short axis and magnetic field direction. (Scale bars: 50 μm)

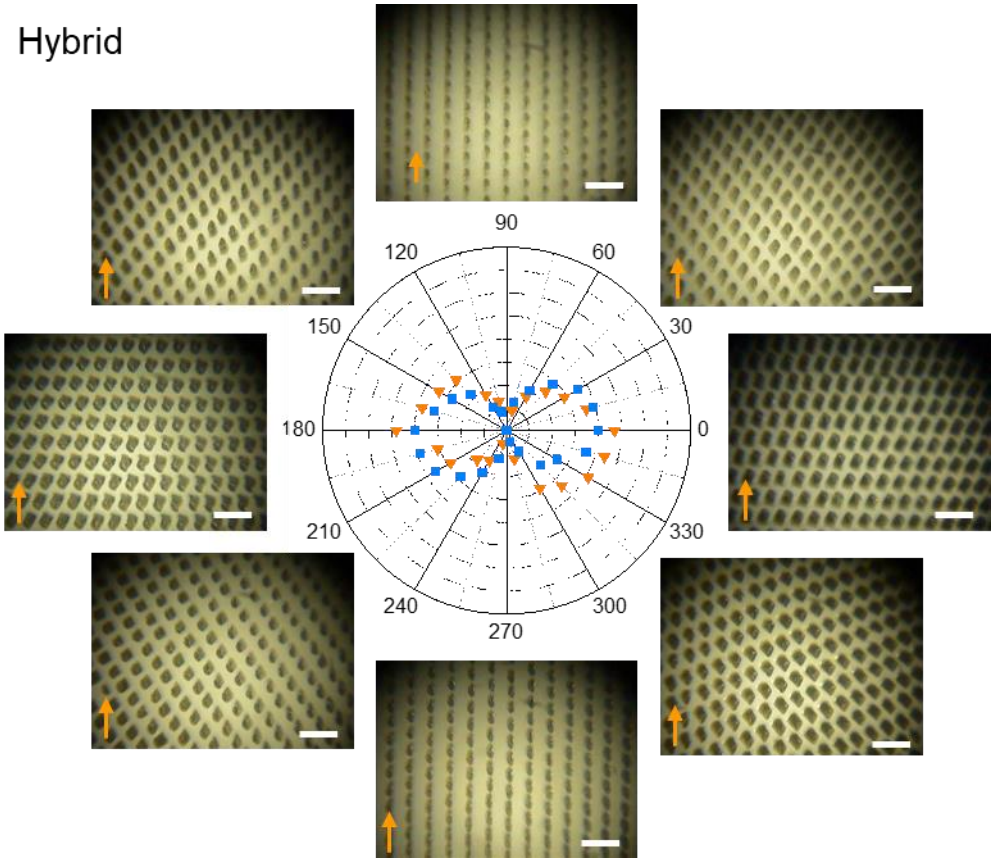


**Figure S16.** The actuation angle variation of hybrid microarray with offset angle. Polar plot of actuation angle of hybrid microarray depends on offset angle between horizontally short axis and magnetic field direction. (Scale bars: 50 μm) (▼: twisting angle, ■: bending angle)

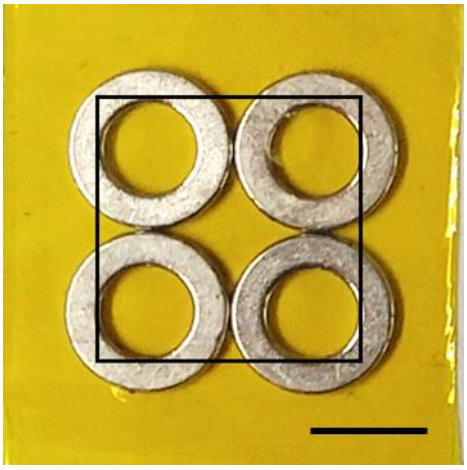

**Figure S17.** The image of quadripolar array. The negative mold located in black square. (Scale bar: 5 mm)

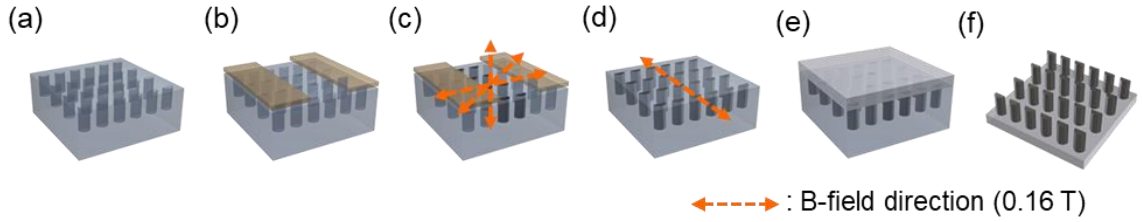


**Figure S18.** Fabrication procedure of arbitrary patterned microarray. (a) Prepare negative PDMS mold, (b) mask with polyimide tape and fill the unmasked area, (c) align the iron particle with external magnetic field and precuring, (d) fill the background area and aligned the particle as a HSA mode, (e) pour pure PDMS and fully cure, and (f) harvest the microarray from PDMS mold.

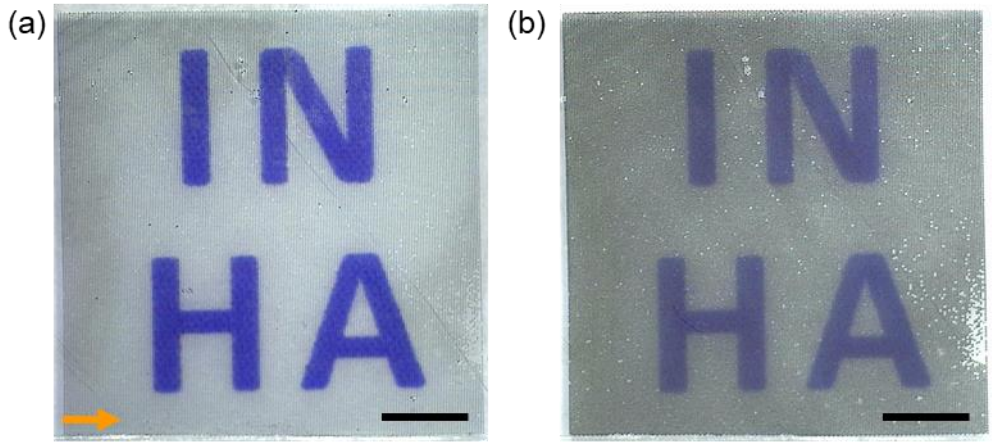


**Figure S19.** Optical difference. (a, b) Digital image of (a) non-actuated and (b) actuated microarrays (Direction of magnetic field: orange arrow, applied magnetic flux density in b: 0.6 T, scale bars: 2 mm)

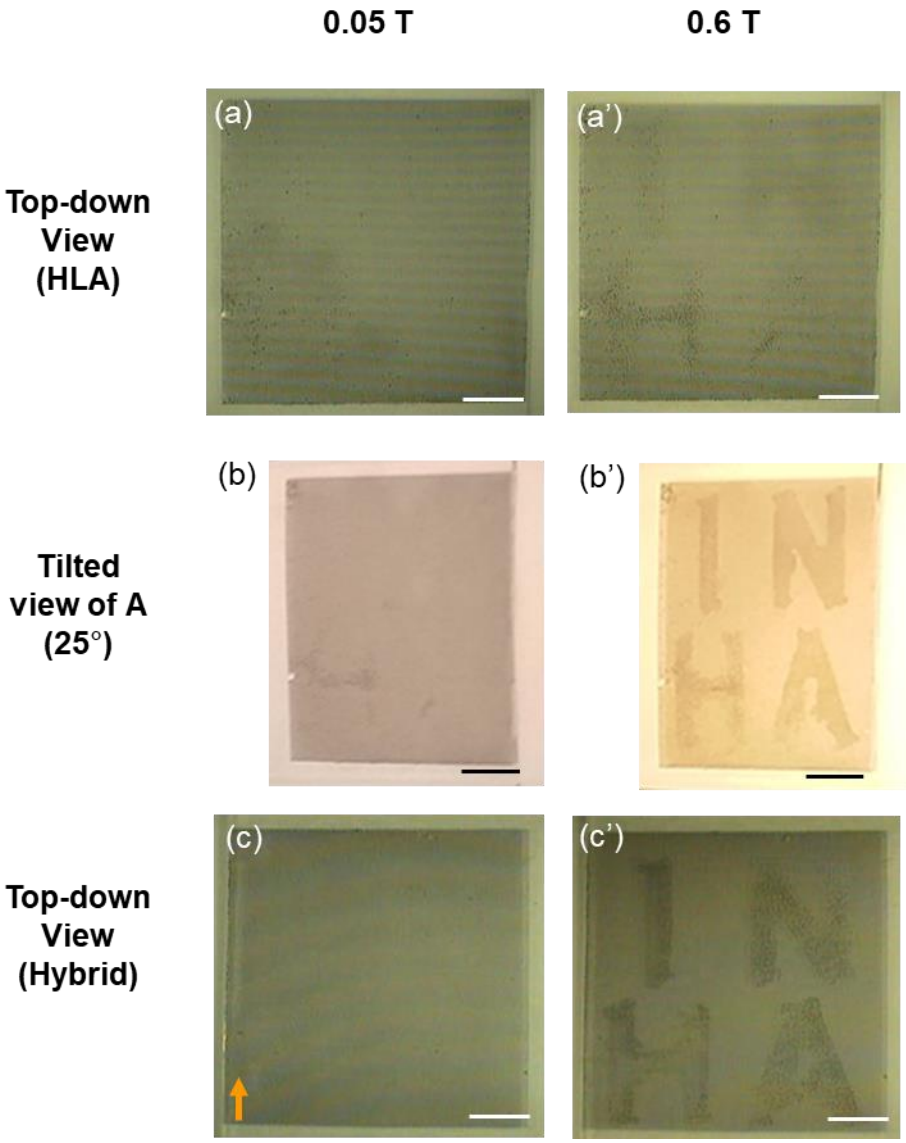


**Figure S20.** Arbitrary patterned actuation of HLA and hybrid microarrays. (a, b, c) Before and (a', b', c') after actuation of various microarrays with arbitrary pattern ('INHA' letters), (a) letter: HLA mode, (b) tilted view of A (25°), (c) letter: hybrid mode, background: HSA mode, (scale bars: 2 mm)

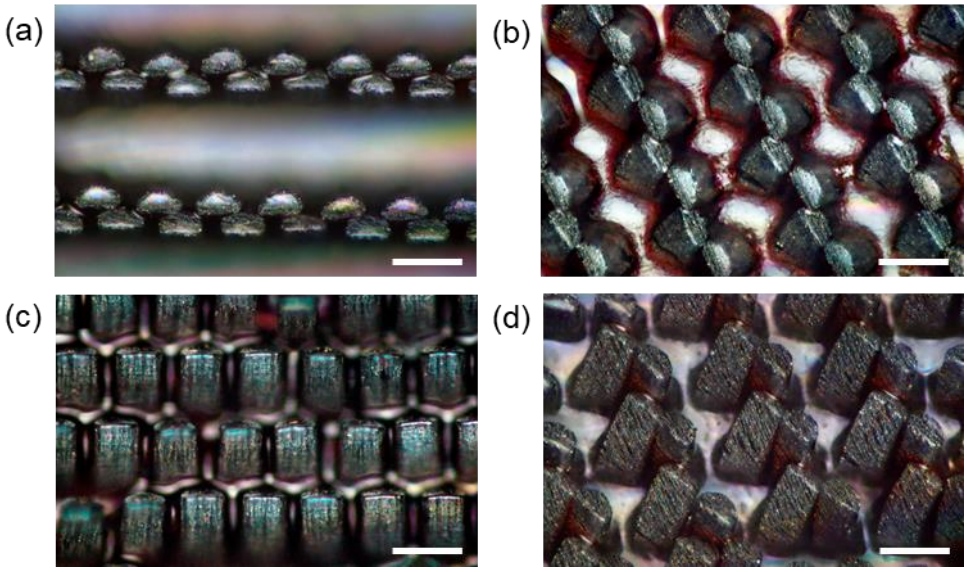


**Figure S21.** The optical micrographs of each self-assembled microarray. (a), HSA microarray. (b), HLA microarray. (c), VA microarray. (d) Hybrid microarray (scale bars: 50 μm)

**Table S1.** Surface coverage of polymer composite micropillars.

| | **Coverage (%)** | | | | |
|---|---|---|---|---|---|
| | **RD** | **HSA** | **HLA** | **VA** | **Hybrid** |
| **0.05 T** | 19.4 | 17.3 | 18.3 | 19.8 | 19.8 |
| **0.6 T** | 27.5 | 17.3 | 26.1 | 61.9 | 51.4 |

**Supporting Movie 1.**

Movie clip of actuation of randomly dispersed (RD) iron particle in microarray. The movie plays at x16 speed in comparison with real-time. The variation of magnetic field is 0.05 T to 0.6 T. Scale bars indicate 50 μm.

**Supporting Movie 2.**

Movie clip of actuation of horizontal short-axis aligned (HSA) iron particle in microarray. The movie plays at x16 speed in comparison with real-time. The variation of magnetic field is 0.05 T to 0.6 T. Scale bars indicate 50 μm.

**Supporting Movie 3.**

Movie clip of actuation of horizontal long-axis aligned (HLA) iron particle in microarray. The movie plays at x16 speed in comparison with real-time. The variation of magnetic field is 0.05 T to 0.6 T. Scale bars indicate 50 μm.

**Supporting Movie 4.**

Movie clip of actuation of vertically aligned (VA) iron particle in microarray. The movie plays at x16 speed in comparison with real-time. The variation of magnetic field is 0.05 T to 0.6 T. Scale bars indicate 50 μm.

**Supporting Movie 5.**

Movie clip of actuation of combination of HLA and VA (hybrid) microarray. The movie plays at x16 speed in comparison with real-time. The variation of magnetic field is 0.05 T to 0.6 T. Scale bars indicate 50 μm.

**Supporting Movie 6.**

Movie clip of concerted actuation of microarray programmed magnetic component via patterned magnetic field. The movie plays at x16 speed in comparison with real-time. The variation of magnetic field is 0.05 T to 0.6 T. Scale bars indicate 100 μm.

**Supporting Movie 7.**

Movie clip of arbitrary patterned actuation (“INHA” letter) of microarray programmed magnetic component via masking technique. The movie plays at x16 speed in comparison with real-time. The variation of magnetic field is 0.05 T to 0.6 T. Scale bars indicate 2 mm.

**Supporting Movie 8.**

Movie clip of on-demand droplet spreading on VA microarray. The movie plays at x2 speed in comparison with real-time. The variation of magnetic field is 0.05 T to 0.6 T. Scale bars indicate 200 μm.

**References**

(1) Park, J. E.; Jeon, J.; Cho, J. H.; Won, S.; Jin, H.-J.; Lee, K. H.; Wie, J. J. Magnetomotility of Untethered Helical Soft Robots. *RSC Adv.* **2019**, *9*, 11272–11280.

(2) Cvek, M.; Torres-Mendieta, R.; Havelka, O.; Urbanek, M.; Plachy, T.; Cernik, M. Laser-Induced Fragmentation of Carbonyl Iron as a Clean Method to Enhance Magnetorheological Effect. *J. Clean. Prod.* **2020**, *254*, 120182.

(3) Bombard, A. J. F.; Joekes, I.; Alcântara, M. R.; Knobel, M. Magnetic Susceptibility and Saturation Magnetization of Some Carbonyl Iron Powders Used in Magnetorheological Fluids. *Mater. Sci. Forum* **2003**, *416–418*, 753–758.

(4) Gere, J. M.; Timoshenko, S. P. Mechanics of Materials; General Engineering Series; *PWS Pub Co.*, **1997**.